Multiplexed Orthogonal Polarizations Harmonic Imaging for Probing Dynamic Biological Processes

Matthew Gleeson, Sophie Escot, Xavier Solinas, Bahar Asadipour, Willy Supatto, Pierre Mahou, Chiara Stringari, Emmanuel Beaurepaire

ACS Photonics

pubs.acs.org/journal/apchd5
Article

Multiplexed Orthogonal Polarizations Harmonic Imaging for Probing Dynamic Biological Processes

Matthew Gleeson, Sophie Escot, Xavier Solinas, Bahar Asadipour, Willy Supatto, Pierre Mahou, Chiara Stringari, and Emmanuel Beaurepaire*

Cite This: https://doi.org/10.1021/acsphotonics.4c00660

ABSTRACT: Polarization-resolved nonlinear optical microscopy can provide label-free images of anisotropic biomaterials. Existing techniques are often limited by their complexity, chromaticity, or slowness. In this article, we propose a simple implementation based on the passive splitting of the excitation beam into slightly delayed orthogonally polarized pulse trains. Label-free second- and third-harmonic signals corresponding to each polarization state are separated by time-resolved photon counting, resulting in the acquisition of image pairs that are automatically registered with submicron spatial precision and nanosecond simultaneity. We demonstrate the utility of this small-footprint approach for live studies by presenting structural imaging of tubulin, myelinated axons, and blood vessels in zebrafish larvae, dynamic imaging of flowing microcrystals in the zebrafish larval otolith cavity, and mitotic spindles in dividing embryonic cells.

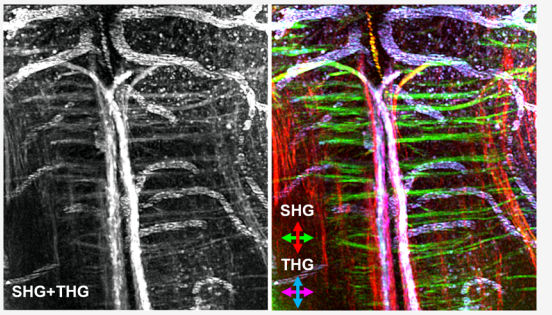

KEYWORDS: *multiphoton microscopy, second harmonic generation, third harmonic generation, polarization, otolith, mitotic spindles, tubulin, myelin*

1. INTRODUCTION

Nonlinear optical (NLO) microscopy is widely used to study biological tissues because it provides submicron resolution and efficient optical sectioning in thick samples. An important feature of NLO microscopy is that it allows label-free imaging based on nonfluorescent contrasts such as second harmonic generation (SHG) and third harmonic generation (THG).[1,2] Biological SHG occurs in organized noncentrosymmetric macromolecular structures such as fibrillar collagen, myofilaments, and polarized microtubule bundles and exhibits a strong dependence on the excitation laser polarization.[3−7] THG occurs at the interface between any two media with different nonlinear susceptibilities or in birefringent materials. THG has been used to image lipidic structures in cells and tissues,[8−10] including myelinated axons,[11] and has also been shown to exhibit polarization sensitivity.[12−15]

Polarization-resolved SHG or THG (pSHG or pTHG) has found several uses in biomedical research.[15−18] However, polarization-resolved setups tend to be complex, require expensive equipment, or are difficult to implement, which limits a wider adoption. Probing the polarized nonlinear response of a sample requires several measurements, and therefore a longer acquisition time than simple intensity imaging. Several experimental approaches have been explored to probe this response. Some implementations have focused on the accuracy and completeness of the polarimetric measurement[19−23] and have not been demonstrated on dynamic samples, while others have focused on increasing the acquisition speed to make them compatible with live imaging. Among the pSHG or pTHG imaging methods favoring speed, some implementations have used an electro-optic modulator (EOM) to switch the polarization state between two lines of an image, achieving a temporal precision of the polarimetric measurement for each pixel in the millisecond range.[14,24] Two limitations of this strategy are that the temporal precision is coupled to the lateral field of view and that it can only operate at a single wavelength because EOMs are chromatic. Other reported implementations have proposed probing the sample with only two polarization states using interleaved pulse trains with orthogonal polarizations. Such methods included the use of a polarizing beam splitter cube (PBSC) and long delay lines to obtain a doubled repetition rate in the excitation pulse train.[25−28] These implementations involve a significant difference in the propagation distance between the two beams, resulting in mismatched resolution and foci. Although this issue can be addressed by using deformable mirrors to control the focal planes, the increased information comes at the cost of

Received: April 9, 2024
Revised: June 12, 2024
Accepted: June 12, 2024

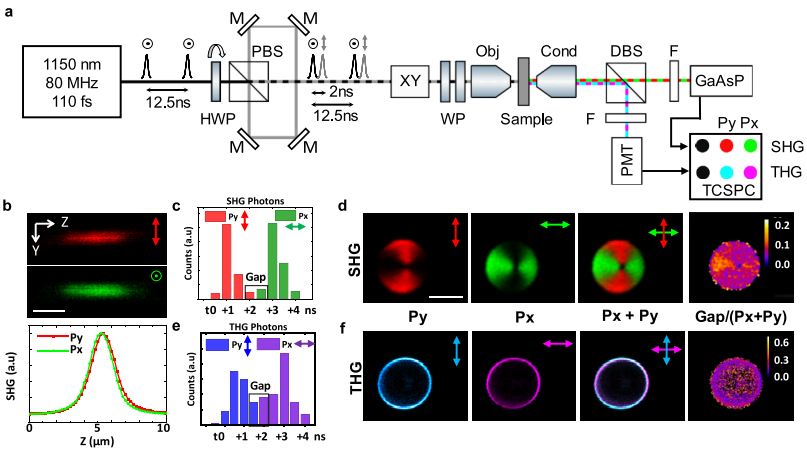

Figure 1. MOrPHIng setup and characterization. (a) Schematic of the microscope. Pairs of pulses with orthogonal polarization and 2 ns temporal separation are generated by a delay loop. Focused pulses are scanned across the sample. SHG-THG signals corresponding to each polarization state are separated by TCSPC detection. Up to four images are acquired simultaneously. HWP: Half wave plate. PBS: Polarizing beamsplitter. M: Mirror. XY: Galvo scanning. WP: Wave plates. Obj: Objective. Cond: Condensor. DBS: Dichroic beamsplitter. F: Filter. (b) YZ projections of SHG from KTP nanoparticles and axial (Z) profiles. Scale bar: 1 μm. (c) Histogram of SHG photon detection times with the GaAsP detector. (d) Corresponding SHG images of a starch granule. Scale bar: 10 μm. (e) Histogram of THG photon detection times with the PMT detector. (f) THG images of the same starch granule as in (d).

a large experimental footprint and increased complexity. Finally, compact passive polarization multiplexing schemes have been proposed to cancel the anisotropy dependence of two-photon microscopy,[29] but they are not compatible with polarization-sensitive detection. Therefore, wider adoption of polarimetric multiphoton microscopy in biomedical sciences still requires the development of more compact, robust, and possibly clinic-friendly setups.

In this letter, we propose a simple technique based on the passive splitting of the excitation beam into orthogonally polarized pairs of pulses separated by a delay in the nanosecond range. Polarization demultiplexing is performed by time-correlated single-photon counting (TCSPC) detection, resulting in two simultaneous images corresponding to each polarization state. This approach, called multiplexed orthogonal polarizations harmonic imaging (MOrPHIng), has a small footprint (15 × 15 cm^2), is simple to align, and can be easily integrated into existing microscopy systems. Excitation with orthogonally polarized pulses can be used either to selectively highlight anisotropic structures or, conversely, to attenuate orientation effects without using circular excitation polarization, which would suppress most THG signals.[12,14] We demonstrate our strategy for in vivo recording of pSHG-pTHG signals in tubulin structures, myelinated axons, and flowing microcrystals.

2. RESULTS AND DISCUSSION

2.1. Optical Setup and Microscope. We chose to implement our technique with the minimum temporal separation of 2 ns between the pulses allowed for by the detection chain. This allows the pulses to be detected independently while minimizing the propagation difference between the two beams, which is a possible source of resolution difference between the two images. MOrPHIng was designed as an add-on module to an existing home-built multiphoton microscope equipped with a femtosecond OPO (80 MHz, 110 fs pulse duration, 1150 nm, Insight DS+, Spectra Physics). Pulse splitting into orthogonally polarized pulse pairs is achieved using a half-waveplate (HWP) oriented at approximately 45°, a PBSC, and a 60 cm loop made of 4 mirrors, as shown in Figure 1a. This setup produces a train of orthogonally polarized pulse pairs separated by 2 ns. The horizontally polarized component of the initial pulse passes straight through, while the vertically polarized component travels around the loop before being recombined with the direct beam. The relative power between the two beams is balanced by adjusting the angle of the HWP to compensate for the losses experienced in the loop and to ensure equal power under the objective. The beams are XY scanned by galvanometric scanners (Cambridge technology). Note that the scanning system rotates the horizontal and vertical polarizations in the microscope by 90°, so that the first pulse in the sequence is polarized along the vertical (Y) axis in the sample plane, called P_y. The second horizontally polarized pulse is called P_x. An HWP before the water immersion objective (25×, 1.05 NA, Olympus Japan) can rotate the polarization pulse orientation within the field of view of the microscope. The waveplate (WP) pair before the objective can reduce beam ellipticity if needed. SHG and THG light is collected in transmission geometry by a condenser (Olympus, NA = 1.4). The excitation light is filtered out by a 705 nm short pass filter (Semrock Brightline multiphoton, FF705-DiO1). SHG and THG are split by a dichroic (Semrock Brightline FF495-DiO3) with bandpass filters for SHG (Semrock Brightline Fluorescence FF01-575/19-25) and THG (Semrock Brightline Fluorescence FF01-390/40-25) placed in front of the detectors. SHG is measured by a GaAsP detector (H7422P-40, Hamamatsu) with an external pulse discriminator (C9744, Hamamatsu). THG is detected by either a GaAsP detector (H7422P-40, Hamamatsu) for Figure 2 or a bialkali PMT (P25PC, SensTech) for Figures 3 and 4. These detectors were chosen for their large sensitive areas which facilitate their alignment and improve the detection of scattered signal light in the case of tissue imaging,[8] but have different sensitivities and temporal characteristics.

A TCSPC detection chain is used to separate the polarization pulses during detection. It is designed in-house using a field-programmable gate array (FPGA, Spartan 6, Xilinx). A digital time converter (TDC) measures the delay

https://doi.org/10.1021/acsphotonics.4c00660
ACS Photonics XXXX, XXX, XXX−XXX

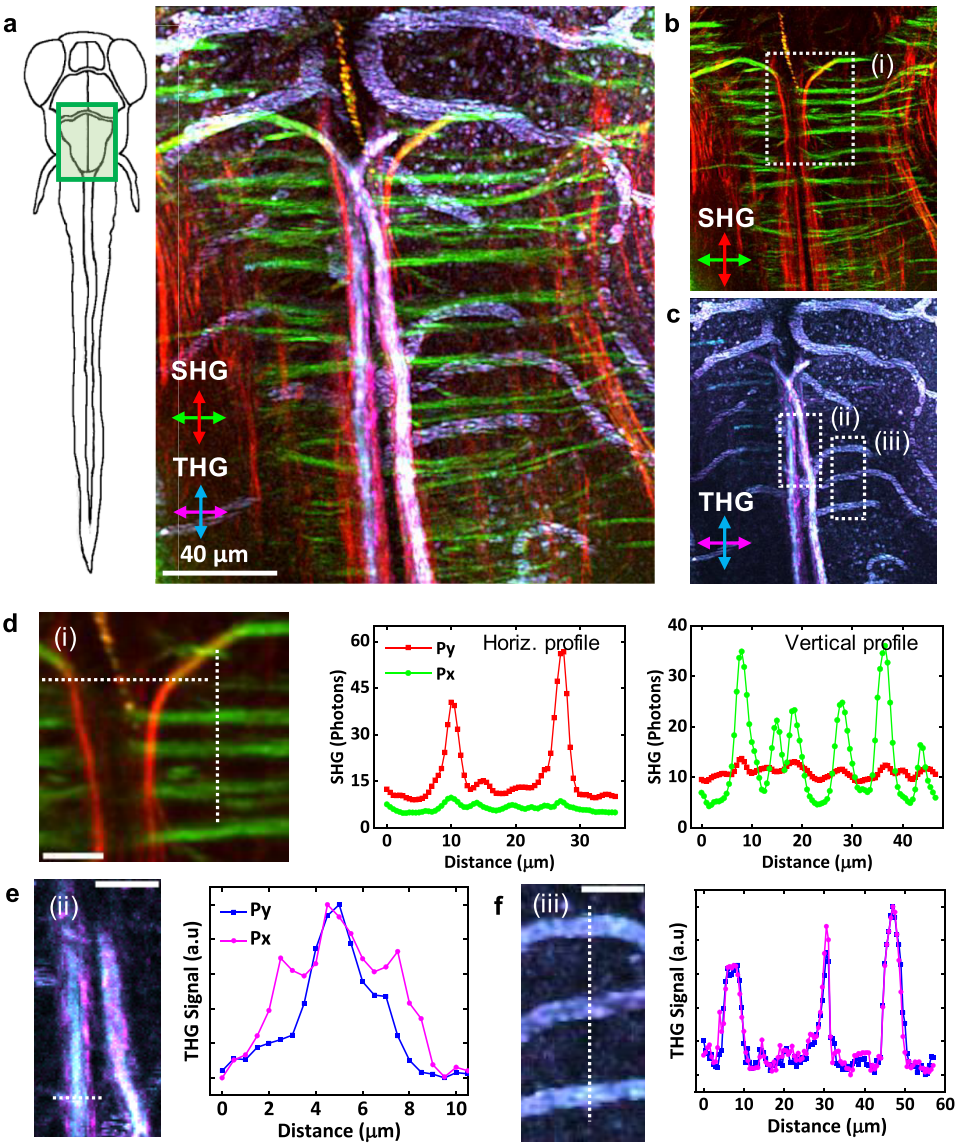

Figure 2. Label-free imaging of microtubulin, Mauthner axons and blood vessels in the brainstem of 5dpf zebrafish. (a) Composite Z-stack image of P_x and P_y SHG/THG polarizations with arbitrary contrast. (b) SHG and (c) THG channels. (d) Enlargement of the dashed box (i) in (b) with line scans at horizontal/vertical locations indicated by the dotted white lines. (e) THG from Mauthner axon with signal profiles along the horizontal dotted line shown for both polarizations. (f) THG from blood vessels with 1 pixel Gaussian blur applied to reduce noise and signal profiles along the vertical dotted line shown for both polarizations. Scale bars in (d, e, f) are 15 μm.

between the excitation laser pulses, with the TCSPC box connected to the laser repetition rate output, and the photons detected by the PMT/GaAsP. The photon counts are sorted by arrival time into 0.52 ns bins, over a time range of 24 bins, for a total possible window of 12.5 ns. The TDC is implemented in the FPGA with two interleaved deserializers clocked at 960 MHz. The photons are then counted according to their arrival time. Integration windows of 2 or 3 bins are used for the P_x and P_y pulses. The photons arriving in the bins between the pulse peaks, called "gap" photons in Figure 1c–f, are discarded to reduce crosstalk between the polarizations. The total number of photons is taken as the number of "gap" photons plus the photons in the P_x and P_y integration windows.

2.2. Spatial and Temporal Characterization. SHG from 150 nm diameter KTiOPO4 (KTP) nanoparticles is used to coalign the orthogonally polarized beams,[30] as shown by the YZ projections and Z scans in Figure 1b. Since the nanocrystals are smaller than the point spread function of the microscope, the overlapping of SHG images from the P_x and P_y polarizations, referred to as the image merging in the following text, indicates submicron accuracy alignment. A Z-scan of the SHG signals shows an axial resolution of approximately 1.8 μm for both beams and a Z-mismatch of approximately 200 nm, indicating that essentially the same plane is probed by both polarization pulses. The spatial overlap and axial resolution across the FOV of the microscope are shown in Supporting Information Figure S1.

We characterized the temporal response and channel separation of our system using SHG-THG images of starch granules. Starch granules contain a semicrystalline stack of radially distributed amylopectin and produce hourglass-shaped SHG images with a maximum obtained in the direction of incident polarization.[31]

https://doi.org/10.1021/acsphotonics.4c00660
ACS Photonics XXXX, XXX, XXX−XXX

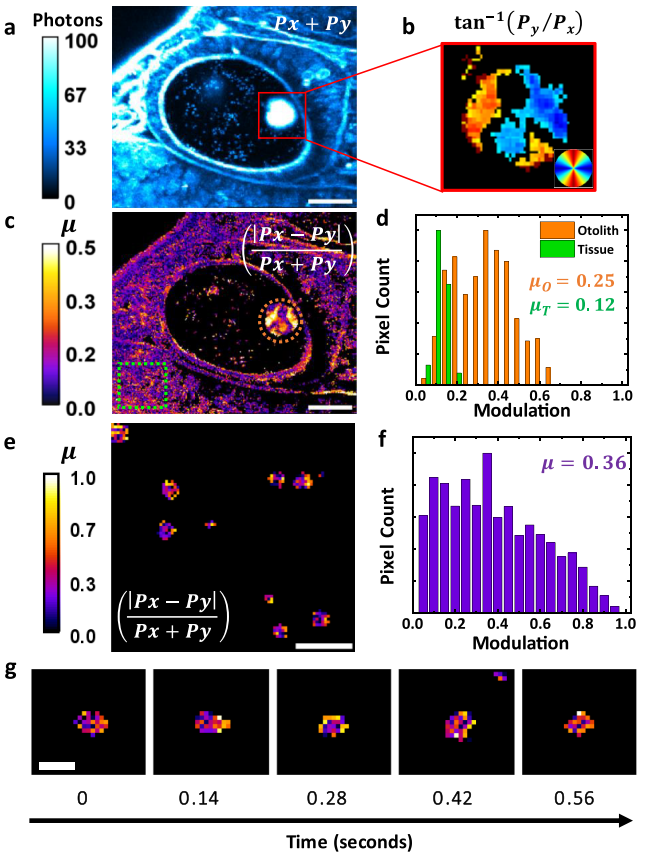

Figure 3. MOrPHIng THG of the otolith and crystalline microparticles in a 2 dpf zebrafish embryo. (a) Sum of P_x and P_y THG images, calibration bar in photon count. (b) Close-up of otolith THG $\tan^{-1}(P_y/P_x)$ after intensity-based thresholding (see text). This representation highlights the presence of several crystalline domains in the otolith. (c) (D/S) of the image gives a simple estimate of the THG dependence on polarization direction. (d) Histogram of (D/S) pixel values for otolith and tissue in image (c), inset values of μ refer to modulation. (e) Frame of (D/S) time-lapse of flowing microparticles within the otolith cavity. (f) Histogram of (D/S) values of microparticles in the otolith cavity. (g) Tracking of a single particle across multiple frames in subregion of (e). Scale bars are 20 μm for (a, b, c), 5 μm in (e) and 2 μm in (g).

We tested two types of detectors with different temporal characteristics. The GaAsP detectors' time transit spread (TTS) of 300 ps allows for a clear separation between the SHG polarizations with few photons registered between the peaks, Figure 1c. Overlaid SHG images, Figure 1d, show the low overlap between the P_y (red) and P_x (green) polarizations. As a measure of the photon utilization efficiency, the last panel shows the ratio of the "gap" photons to the total number of photons detected. The mean value of the gap to total within the granule is 7.3% ± 2.3%, indicating an efficiency of more than 90% due good temporal characteristics of the GaAsP detectors. PMTs are slightly less sensitive and have a higher TTS compared to GaAsP detectors, but their higher durability and larger sensitive area are beneficial for wider utility. In Figure 1e, we can see that the gap between the polarization pulses is more populated compared to the GaAsP detector. THG images of the P_y (cyan) and P_x (magenta) polarizations across a starch granule interface, Figure 1f, have a higher overlap compared to the GaAsP. The mean pixel value of the gap over the total number of photons within the starch is 16% ± 11%. The PMT photon utilization efficiency is approximately 80%. We note that the temporal detection uncertainty could in principle be reduced by several methods. Replacing the leading edge timing discriminator with a constant fraction discriminator which would be less sensitive to variations in detector gain. Alternatively, by using a more accurate TDC or by using detectors with smaller TTS.

2.3. Zebrafish Embryo Preparation for Imaging. Embryos were obtained by the natural spawning of wild-type AB adult fishes and incubated at 28 °C. Five days post fertilization (dpf) embryos, Figure 2, were mounted in a dorsal orientation and fixed in place with agarose. Two dpf embryos, Figure 3, were mounted in a lateral orientation and fixed with agarose. For imaging early divisions, Figure 4, one-cell stage embryos were dechorionated in embryo medium and mounted in 0.5% low melting agarose. All embryos were transferred to plastic dishes with a glass coverslip bottom, then the dish was filled with a mixture of tricaine and embryo water to facilitate the use of a water immersion objective. One-cell stage embryos were oriented with the cells up and the first cell division aligned with the X-axis of the microscope field of view. All animal experiments were performed in accordance with the local ethics committee and approved by the Ethics Committee N°59 and the Ministère de l'Education Nationale, de l'Enseignement Supérieur et de la Recherche.

2.4. Selective Imaging of Myelinated Axons, Tubulin, and Blood Vessels in the Brainstem of Live Zebrafish Larvae. As a first illustration of the additional information, compared to single polarization or intensity imaging, provided by the MOrPHIng approach, we recorded simultaneous label-free SHG-THG images in the brainstem of zebrafish larvae at 5 dpf, shown in Figure 2a. After discarding the gap photons as described above, typical signal levels for all visible structures are 100−120 photons in THG and 10−60 photons in SHG with an incident power of 65 mW in each polarization and a pixel dwell time of 20 μs. The SHG channel, Figure 2b, reveals a set of structures oriented along the medio-lateral and anteroposterior axes of the embryo, dashed box (i). These SHG signals are significantly weaker than those produced by collagen and muscle fibers and instead correspond to polarized bundles of microtubules.[7,32] These are probably commissural axonal projections of hindbrain interneurons (for comparison, see e.g. Figure 4 in ref 33). Consistent with the tubulin origin of these SHG signals, a strong dependence on incident polarization is observed, with the maximum signal obtained when polarization is parallel to these fibers. MOrPHIng not only reveals these structures but also their polarization dependence. Intensity profiles for both polarizations along the horizontal and vertical directions are shown in Figure 2d. With our detection conditions, we obtained a contrast greater than 5 in both SHG images.

Simultaneously acquired THG images reveal other structures such as the Mauthner axons, dashed box (ii), and red blood cells, dashed box (iii), in Figure 2c. Blood vessels are revealed by the presence of red blood cells, which have a strong three-photon resonant THG signal.[34] Mauthner axons, the largest axons present in the larval brainstem, have a lipidic myelin sheath approximately 200 nm thick, making them particularly visible in THG images.[11,35] Remarkably, we observed that the THG response of these axons depends on the orientation of the incident polarization relative to the axon, Figure 2e. This dependence is not present in THG from red blood cells, Figure 2f, where the line profiles for orthogonal

https://doi.org/10.1021/acsphotonics.4c00660
ACS Photonics XXXX, XXX, XXX−XXX

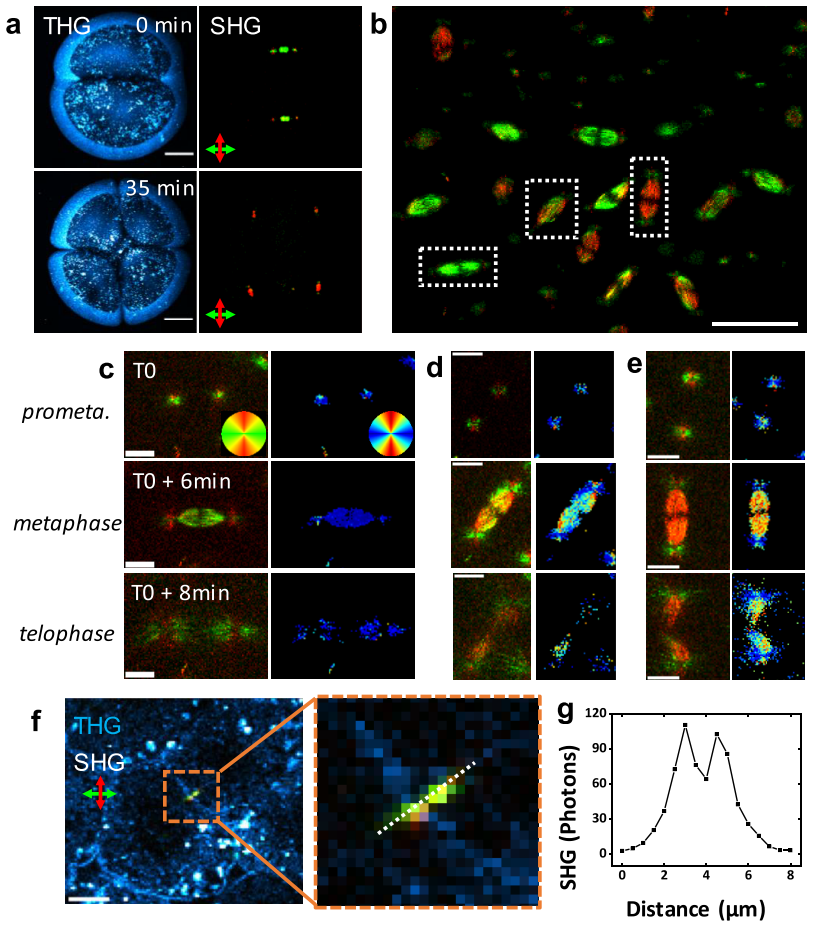

Figure 4. Mitotic spindle evolution. (a) Division from 2 cell to 4 cell stage of zebrafish embryo with ($P_x + P_y$) THG (cyan), P_x SHG (green) and P_y SHG (red). The contrast settings have been stretched for the sake of presentation. Scale bar: 100 μm. (b) Later stage divisions approximately 3 h post fertilization show multiple spindle orientations. Scale bar: 50 μm. (c–e) Close up of mitotic spindle centrosome cycle for various spindle orientations imaged simultaneously, shown in Supplementary Movie M3. (f) Intercellular bridge generates strong SHG across cell walls seen in THG. Scale bar: 10 μm. (g) Profile of ($P_x + P_y$) SHG along the intercellular bridge shown in zoom of panel (f). Left columns of (c–e) are the merged P_x and P_y channels, right columns are $\tan^{-1}(P_y/P_x)$. Scale bars in (c–e) are 5 μm.

polarizations are nearly identical. Thus, the simultaneous acquisition of two THG images corresponding to orthogonal polarizations makes it possible to distinguish signals from blood vessels from those from myelinated axons. This first demonstration clearly illustrates how multiharmonic MOrPHIng can provide a wealth of label-free structural information in nerve tissue, and the benefits of polarization-sensitive imaging for structural analysis.

2.5. Imaging of Biomineralization and Flowing Crystalline Particles. We then explored the potential of MOrPHIng to probe biomineralization *in vivo* by recording THG movies of the otolith cavity of a 2 dpf zebrafish embryo. The otoliths are mineralized structures involved in orientation and gravity sensing. They are primarily composed of crystalline calcium carbonate and initially grow by aggregation of precursor microparticles moving in a cilia-driven flow in the otolith cavity.[36] Figure 3a shows the sum of the P_x and P_y THG images of the otolith cavity. The otolith itself is a particularly efficient THG source compared to most surrounding tissue structures and is shown as a saturated signal in the image. Flowing microparticles are also visible within the cavity (see also Supplementary Movie M1). The THG image reveals several other structures in the surrounding tissue, and intensity alone does not provide very specific identification. However, the polarimetric information provided by MOrPHIng, even if incomplete, can be used to calculate parameters that reveal the anisotropic nature of different materials. For example, Figure 3b shows the pseudoangle calculated with $\tan^{-1}(P_y/P_x)$. This approximation maps these values onto the inset color wheel from blue to red, where blue indicates a horizontal direction and red indicates a vertical direction. After applying an intensity-based threshold to remove the weakest signals, this image reveals that the otolith is made up of several crystal domains with different orientations relative to the excitation polarizations.

A complementary analysis is to use the absolute difference (D) between the P_x and P_y components divided by their sum (S), i.e., $|P_x - P_y|/(P_x + P_y)$.[26] This metric applied to the otolith cavity and surrounding tissue is shown in Figure 3c. In contrast to Figure 3b, this calculation removes the signal dependence on the relative orientation between crystalline axes and excitation polarizations. Instead, it provides a simple estimate of the polarization sensitivity (later called "modulation" or μ) that can be used to distinguish between hard minerals such as the otolith and the surrounding soft tissue. The otolith stone has a peak modulation of approximately 0.5 and the surrounding soft tissue has a peak modulation of approximately 0.1. The histogram in Figure 3d quantifies the

https://doi.org/10.1021/acsphotonics.4c00660
ACS Photonics XXXX, XXX, XXX−XXX

modulation values for pixels recorded in the otolith and soft tissue within the dashed boxes shown in Figure 3c. The otolith has a higher mean modulation of 0.25 compared to the surrounding soft tissue of 0.12.

MOrPHIng is also compatible with the rapid motion (1−50 μm/s) of the otolith precursor microparticles flowing in the cavity, Figure 3e and Supplementary Movie M1. Using the (D/S) approximation introduced above, the mean THG modulation of the microparticles is measured to be 0.36, as shown in Figure 3f. This is in good agreement with more complete polarimetric measurements performed with 4 polarization states,[14] without the need for an electro-optical modulator for fast polarization control. For a 20 μm^2 area with 0.25 μm pixel size and a pixel time of 20 μs, frames like Figure 3e are acquired every 0.14 s. In the time-lapse Movie, Supplementary Movie M1, the motion of individual particles can be tracked over multiple frames, Figure 3g. Changes in (D/S) pixel values for individual particles in successive frames are likely due to noise or the rotational motion of the particles during acquisition.

This experiment and subsequent analysis show that the MOrPHIng approach can identify anisotropic materials in THG images of living tissue and distinguish between adjacent crystalline microdomains that have different orientations. Although the polarimetric information obtained is not complete, the simultaneity of the measurement makes it possible to characterize microparticle anisotropy in turbulent dynamic environments.

2.6. Imaging Mitotic Spindle Dynamics in the Early Zebrafish Embryo. SHG-THG microscopy can be used to monitor cell divisions and detect mitotic spindles during early divisions in zebrafish embryos at the blastula stage.[9] We explored the ability of MOrPHIng to provide more precise information on the spindle structure while being compatible with dynamic imaging. In Figure 4a, we acquired an XYZT scan with a voxel size of 2 × 2 × 2 μm^3 over a depth of 35 μm at time intervals of 2 min. The cell walls and interiors are imaged with THG, while the mitotic spindles, made from arrays of microtubules that switch from horizontal at the two-cell stage, to vertical at the 4-cell stage, are imaged with SHG.[9]

The THG images reveal the cell shapes and internal lipid vesicles, while the SHG image shows the transient formation of the mitotic spindles that separate chromatin during cell division. The spindles consist of polarized assemblies of tubulin, making them SHG sources with a strong dependence on the incident polarization direction. The first series of divisions are highly stereotyped. As the embryo develops from the one-cell to the 16-cell stage, divisions occur in synchronous waves oriented in successive orthogonal directions to form a single layer of cells.[9] Spindles are also sequentially oriented in orthogonal directions. As shown in Figure 4a, MOrPHIng efficiently detects the X-orientation of spindle microtubules during the 2−4 division cycle and their orthogonal Y-orientation during the 4−8 division cycle, without the need to change the polarization direction of the laser.[5] A greater variety of spindle orientations is present at later stages, Figure 4b and Supplementary Movie M2. Zooming in on individual spindles at different orientations, Figure 4c−e confirms that microtubule orientation can be probed for all spindles.

Although MOrPHIng uses only two polarization states and does not provide unambiguous angle determination, it can be used to monitor spindle dynamics and probe their internal organization. Successive phases of the mitotic cycle can be seen in the images Figure 4c−e and Supplementary Movie M3. During the prometaphase (top row), the SHG signal increases as microtubules align to form spindles. SHG intensity reaches its maximum during the metaphase (middle row) as microtubule density increases. The absence of SHG signals at the midline of the spindles is due to antiparallel alignment of the microtubules, resulting in destructive interference. Finally, during the telophase (bottom row), the SHG signal decreases as spindles uncondense and tubulin disperses throughout the cell.[5,37]

A simple merge of the P_y (red) and P_x (green) images is shown in the left columns of Figure 4c−e, while the pseudo angle $\tan^{-1}(P_y/P_x)$ metric introduced above is shown on the right of the columns. Note that this approximation is limited to strongly anisotropic materials such as microtubule arrays with two-lobe pSHG angular profiles.[7] Having only two excitation polarizations is insufficient to determine the angular distribution for materials such as myosin or collagen which have more complex pSHG profiles.[7] Nevertheless, this data demonstrates that MOrPHIng can report not only on the average orientation of microtubules within spindles but also on spindle structure and its evolution during the cell cycle. The distinct orientation of the polar microtubules located between the centrosomes and the astral microtubules located on the outside of the mitotic apparatus is detected, as well as the angular distribution of the polar microtubules. As the telophase ends and the daughter cells separate, an intercellular bridge (ICB) containing microtubules is formed across the cell membrane.[38] Combined SHG/THG images, Figure 4f shows that the microtubules are oriented perpendicular to the cell interface. The center of the ICB is marked by the midbody, where the microtubules switch from parallel outside the midbody to antiparallel inside the midbody and where no SHG is generated.[39] This is reflected in Figure 4g where an M-shape line scan is recorded along the ICB showing a dip in SHG across the midbody. This subtle variation of the ICB SHG profile has not been previously reported, let alone in dynamic imaging, and illustrates that our approach is compatible with the detection of small polarized harmonic signals within microsecond pixel times in a live context.

3. CONCLUSIONS

We have proposed a simple and effective way to integrate polarization-sensitive contrast into a SHG-THG microscope. MOrPHIng is based on excitation with pairs of orthogonal polarization pulses separated by nanosecond delays and temporal demultiplexing by time-resolved photon counting. MOrPHIng offers a number of advantages over previous schemes reported in the literature for fluorescence imaging,[25−29] particularly for applications on harmonic imaging of dynamic samples. The small optical path difference between the two beams guarantees similar resolution and Z location for both images without the need for additional optics, and results in a nanosecond temporal resolution of the polarimetric measurements. The small footprint of the MOrPHIng setup also maintains compatibility with most point-scanning microscope geometries. We note that an alternative detection approach could be to resolve the polarization of the harmonic signals on pairs of detectors. Such a strategy may prove more complex to implement on an existing system due to the need for additional detector(s). It would provide a different and possibly complementary measurement based on probing the emission polarization rather than the signal dependence on the

https://doi.org/10.1021/acsphotonics.4c00660
ACS Photonics XXXX, XXX, XXX−XXX

excitation polarization as in MOrPHIng. We also note that an obvious limitation of our method is that it probes the sample response to only two polarization states. We have shown, however, that the information gained over nonpolarization-resolved harmonic microscopy is very significant, whether for structural imaging of immobile tissues or for imaging of dynamic objects. It should also be noted that MOrPHIng cannot be used to obtain polarization-resolved imaging of fluorescence signals with emission times of several nanoseconds. However, it can be used to provide efficient excitation with crossed polarizations and to suppress polarization dependence in cases where it is considered an artifact.[29]

In conclusion, probing the polarization dependence of biomaterials adds valuable structural information to SHG and THG microscopy, but can require complex instrumentation and alignment. We have proposed a relatively simple achromatic scheme with excellent temporal resolution and a small footprint that is applicable to weak signals in polarization-resolved harmonic imaging while maintaining compatibility with most scanning microscope setups and imaging environments.

■ ASSOCIATED CONTENT

Supporting Information

The Supporting Information is available free of charge at https://pubs.acs.org/doi/10.1021/acsphotonics.4c00660.

Figure illustrating the spatial overlap of pulses and characterization of the PSF (PDF)

Particle motion in the interior of otolith cavity (MP4)

Mitotic spindle divisions in zebra fish embryo (MP4)

Centrosome lifecycle in X, XY, and Y-orientated mitotic spindles (MP4)

■ AUTHOR INFORMATION

Corresponding Author

Emmanuel Beaurepaire − *Laboratory for Optics and Biosciences, École Polytechnique, CNRS, Inserm, Institut Polytechnique de Paris, 91128 Palaiseau, France;* orcid.org/0000-0002-2082-8214; Email: emmanuel.beaurepaire@polytechnique.edu

Authors

Matthew Gleeson − *Laboratory for Optics and Biosciences, École Polytechnique, CNRS, Inserm, Institut Polytechnique de Paris, 91128 Palaiseau, France;* orcid.org/0009-0009-0551-1153

Sophie Escot − *Laboratory for Optics and Biosciences, École Polytechnique, CNRS, Inserm, Institut Polytechnique de Paris, 91128 Palaiseau, France*

Xavier Solinas − *Laboratory for Optics and Biosciences, École Polytechnique, CNRS, Inserm, Institut Polytechnique de Paris, 91128 Palaiseau, France;* orcid.org/0000-0002-2459-4312

Bahar Asadipour − *Laboratory for Optics and Biosciences, École Polytechnique, CNRS, Inserm, Institut Polytechnique de Paris, 91128 Palaiseau, France;* orcid.org/0000-0002-2737-5289

Willy Supatto − *Laboratory for Optics and Biosciences, École Polytechnique, CNRS, Inserm, Institut Polytechnique de Paris, 91128 Palaiseau, France;* orcid.org/0000-0002-4562-9166

Pierre Mahou − *Laboratory for Optics and Biosciences, École Polytechnique, CNRS, Inserm, Institut Polytechnique de Paris, 91128 Palaiseau, France;* orcid.org/0000-0003-4452-1011

Chiara Stringari − *Laboratory for Optics and Biosciences, École Polytechnique, CNRS, Inserm, Institut Polytechnique de Paris, 91128 Palaiseau, France;* orcid.org/0000-0002-0550-7463

Complete contact information is available at: https://pubs.acs.org/10.1021/acsphotonics.4c00660

Author Contributions

M.G., C.S., W.S., and E.B. designed the study. M.G., P.M., C.S., and E.B. optimized the microscopy setup. X.S. implemented the photon-counting electronics. S.E. and B.A. prepared the zebrafish embryos. M.G. performed the experiments and analyzed the data. M.G., C.S., and E.B. wrote the manuscript with input from all other authors.

Funding

Agence Nationale de la Recherche (ANR-EQPX-0029, ANR-10-INBS-04), Fondation Bettencourt-Schueller (Brain Harmonics).

Notes

The authors declare no competing financial interest.

■ ACKNOWLEDGMENTS

We thank Nicolas Olivier, Marie-Claire Schanne-Klein, and Joséphine Morizet for discussions on polarized nonlinear microscopy.

■ REFERENCES

(1) James, D. S.; Campagnola, P. J. Recent Advancements in Optical Harmonic Generation Microscopy: Applications and Perspectives. *BME Front.* **2021**, *2021*, No. 3973857.

(2) Aghigh, A.; et al. Second harmonic generation microscopy: a powerful tool for bio-imaging. *Biophysical Reviews* **2023**, *15* (1), 43−70.

(3) Patrick Christian, S.; et al. Polarization-dependent optical second-harmonic imaging of rat-tail tendon. *J. Biomed. Opt.* **2002**, *7* (2), 205−214.

(4) Duboisset, J.; et al. Generic model of the molecular orientational distribution probed by polarization-resolved second-harmonic generation. *Physical Review A* **2012**, *85* (4), No. 043829.

(5) Bancelin, S.; et al. Probing microtubules polarity in mitotic spindles in situ using Interferometric Second Harmonic Generation Microscopy. *Sci. Rep.* **2017**, *7* (1), 6758.

(6) Raoux, C.; et al. Quantitative structural imaging of keratoconic corneas using polarization-resolved SHG microscopy. *Biomedical Optics Express* **2021**, *12* (7), 4163−4178.

(7) Asadipour, B.; et al. Modeling and Predicting Second-Harmonic Generation from Protein Molecular Structure. *Physical Review X* **2024**, *14* (1), No. 011038.

(8) Débarre, D.; et al. Imaging lipid bodies in cells and tissues using third-harmonic generation microscopy. *Nature Methods* **2006**, *3* (1), 47−53.

(9) Olivier, N.; et al. Cell Lineage Reconstruction of Early Zebrafish Embryos Using Label-Free Nonlinear Microscopy. *Science* **2010**, *329* (5994), 967−971.

(10) Weigelin, B.; Bakker, G. J.; Friedl, P. Third harmonic generation microscopy of cells and tissue organization. *J. Cell Sci.* **2016**, *129* (2), 245−255.

(11) Farrar, M. J.; et al. In vivo imaging of myelin in the vertebrate central nervous system using third harmonic generation microscopy. *Biophys. J.* **2011**, *100* (5), 1362−1371.

(12) Oron, D.; Tal, E.; Silberberg, Y. Depth-resolved multiphoton polarization microscopy by third-harmonic generation. *Opt. Lett.* **2003**, *28* (23), 2315−2317.
(13) Zimmerley, M.; et al. Probing Ordered Lipid Assemblies with Polarized Third-Harmonic-Generation Microscopy. *Physical Review X* **2013**, *3* (1), No. 011002.
(14) Morizet, J.; et al. High-speed polarization-resolved third-harmonic microscopy. *Optica* **2019**, *6* (3), 385−388.
(15) Gleeson, M.; et al. Kidney Stone Classification Using Multimodal Multiphoton Microscopy. *ACS Photonics* **2023**, *10*, 3594−3604.
(16) Golaraei, A.; et al. Changes of collagen ultrastructure in breast cancer tissue determined by second-harmonic generation double Stokes-Mueller polarimetric microscopy. *Biomedical Optics Express* **2016**, *7* (10), 4054−4068.
(17) Campbell, K.; et al. Polarization-resolved second harmonic generation imaging of human ovarian cancer. *J. Biomed. Opt.* **2018**, *23* (6), No. 066501.
(18) Raoux, C.; et al. Unveiling the lamellar structure of the human cornea over its full thickness using polarization-resolved SHG microscopy. *Light Sci. Appl.* **2023**, *12* (1), 190.
(19) Kontenis, L.; et al. Third-harmonic generation Stokes-Mueller polarimetric microscopy. *Optics Express* **2017**, *25* (12), 13174−13189.
(20) Dubreuil, M.; Rivet, S.; Le Grand, Y. Snapshot second-harmonic generation polarimeter based on spectral analysis. *Opt. Lett.* **2017**, *42* (22), 4639−4642.
(21) Romijn, E. I.; et al. Automated calibration and control for polarization-resolved second harmonic generation on commercial microscopes. *PLOS ONE* **2018**, *13* (4), No. e0195027.
(22) Gleeson, M.; et al. Quantitative Polarization-Resolved Second-Harmonic-Generation Microscopy of Glycine Microneedles. *Adv. Mater.* **2020**, *32* (46), No. 2002873.
(23) Lee, M.-X.; et al. Calibrated $\chi(2)$-tensor polarization-resolved second harmonic generation microscopy for precise tissue imaging. *Appl. Phys. Lett.* **2023**, *123* (13), No. 133703.
(24) Ducourthial, G.; et al. Monitoring dynamic collagen reorganization during skin stretching with fast polarization-resolved second harmonic generation imaging. *J. Biophotonics* **2019**, *12* (5), No. e201800336.
(25) Amir, W.; et al. Simultaneous imaging of multiple focal planes using a two-photon scanning microscope. *Opt. Lett.* **2007**, *32* (12), 1731−1733.
(26) Sandkuijl, D.; et al. Differential microscopy for fluorescence-detected nonlinear absorption linear anisotropy based on a staggered two-beam femtosecond Yb:KGW oscillator. *Biomedical Optics Express* **2010**, *1* (3), 895−901.
(27) Field, J. J.; et al. Differential Multiphoton Laser Scanning Microscopy. *IEEE Journal of Selected Topics in Quantum Electronics* **2012**, *18* (1), 14−28.
(28) Samim, M.; et al. Differential Polarization Nonlinear Optical Microscopy with Adaptive Optics Controlled Multiplexed Beams. *International Journal of Molecular Sciences* **2013**, *14*, 18520−18534.
(29) Pulin, M.; et al. Orthogonally-polarized excitation for improved two-photon and second-harmonic-generation microscopy, applied to neurotransmitter imaging with GPCR-based sensors. *Biomedical Optics Express* **2022**, *13* (2), 777−790.
(30) Mahou, P.; et al. Metrology of Multiphoton Microscopes Using Second Harmonic Generation Nanoprobes. *Small* **2017**, *13* (42), No. 1701442.
(31) Psilodimitrakopoulos, S.; et al. Starch granules as a probe for the polarization at the sample plane of a high resolution multiphoton microscope. *Proc. SPIE* **2008**, *6860*, 65−75.
(32) Dombeck, D. A.; et al. Uniform polarity microtubule assemblies imaged in native brain tissue by second-harmonic generation microscopy. *Proc Natl Acad Sci U S A* **2003**, *100* (12), 7081−7086.
(33) Roshan, A. J.; et al. Mirror Movement-Like Defects in Startle Behavior of Zebrafish dcc Mutants Are Caused by Aberrant Midline Guidance of Identified Descending Hindbrain Neurons. *J. Neurosci.* **2014**, *34* (8), 2898.
(34) Ferrer Ortas, J.; et al. Label-free imaging of red blood cells and oxygenation with color third-order sum-frequency generation microscopy. *Light Sci. Appl.* **2023**, *12* (1), 29.
(35) Lim, H.; et al. Label-free imaging of Schwann cell myelination by third harmonic generation microscopy. *Proc Natl Acad Sci U S A* **2014**, *111* (50), 18025−18030.
(36) Wu, D.; et al. Mechanistic Basis of Otolith Formation during Teleost Inner Ear Development. *Developmental Cell* **2011**, *20* (2), 271−278.
(37) Yu, C.-H.; et al. Measuring Microtubule Polarity in Spindles with Second-Harmonic Generation. *Biophys. J.* **2014**, *106* (8), 1578−1587.
(38) Schiel, J. A.; et al. Endocytic membrane fusion and buckling-induced microtubule severing mediate cell abscission. *Journal of Cell Science* **2011**, *124* (9), 1411−1424.
(39) Andrade, V.; Echard, A. Mechanics and regulation of cytokinetic abscission. *Front. Cell Dev. Biol.* **2022**, *10*, No. 1046617.

https://doi.org/10.1021/acsphotonics.4c00660
ACS Photonics XXXX, XXX, XXX−XXX